

The Overlapping Control Volume Finite Element Method for Multi-Phase Porous Media Flow Modelling

Part II: Applications

D. Pavlidis^{a,*}, J.L.M.A. Gomes^b, J.R. Percival^a, P. Mostaghimi^a, P. Salinas^a, Z. Xie^a, C.C. Pain^a, M. D. Jackson^a, M. Blunt^a

^a*Applied Modelling and Computation Group, Department of Earth Science and Engineering, Imperial College London, UK*

^b*Environmental & Industrial Fluids Mechanics Group, School of Engineering, University of Aberdeen, UK*

Abstract

This paper is the second part of a two-part paper on a novel finite element method FEM-based formulation for simulating multi-phase flows through porous media. In the first paper, the formulation, based upon the overlapping control volume finite element method, was developed and, simple validation test-cases were presented. In this second paper, the OCVFEM formulation is applied to a set of multi-phase porous media flows test-cases to assess the performance and numerical accuracy of continuous and discontinuous (between elements) element pairs. The test cases include structured and unstructured (triangular / tetrahedral) meshes, as well as heterogeneous problems with large permeability ratios. Numerical solutions are in good agreement with (semi-)analytically obtained data.

Keywords: Multi-phase porous media flow, overlapping control volume finite element method.

1. Introduction

This is the second part of a two part paper developing and applying novel computational methods for multi-phase flow in porous media. The

*Corresponding author.

Email address: dimitrios.pavlidis@imperial.ac.uk (D. Pavlidis)

new overlapping control volume finite element method was introduced in the first part of this paper ([Gomes et al., 2013](#)).

This paper focuses on exploring, by numerical simulations of multi-phase flow in porous media, the fidelity of the results yielded by the continuous pressure (P_n DG- P_{n+1}) and discontinuous pressure (P_n DG- P_n DG and P_{n+1} DG- P_n DG) families of finite element (FE) types introduced in the first paper. By presenting numerical experiments in 1-, 2- and 3-D, we shall study the accuracy, reliability and convergence rates yielded from the proposed FE families for modelling multi-phase displacements in porous media. In this way, quadratic and linear elements are tested for different geometries, meshes and permeability fields. The methods show in all cases good behaviour and a veracious representation of the fluid flow.

The remainder of this paper is organised as follows. A brief description of the model is given in Section 2 followed by the model validation against analytical solutions of the classical Buckley-Levrett problem. In Section 4, water-flood problems (i.e., immiscible fluids displacement) are simulated in 2-D to assess the flow behaviour in heterogeneous porous media. The impact of large permeability ratios (i.e., highly heterogeneous porous matrix) in the model is investigated in Sections 5, 6 and 7. Additionally, in Section 6 the model performance when elements are skewed due to large domain aspect ratio is investigated. A brief summary of the results are presented in Section 8 followed by many conclusions drawn from the two inter-linked papers.

2. Summary of the Model Formulation

The extended Darcy's law and phase saturation equations for N_p immiscible fluid phases can be expressed as:

$$\underline{\underline{\sigma}}_\alpha \mathbf{u}_\alpha := S_\alpha \left(\frac{\mathbf{K} \mathcal{K}_{r_\alpha}}{\mu_\alpha} \right)^{-1} \mathbf{u}_\alpha = -\nabla p + \mathbf{s}_{u_\alpha}, \quad (1)$$

$$\phi \frac{\partial S_\alpha}{\partial t} + \nabla \cdot (\mathbf{u}_\alpha S_\alpha) = s_{\text{cty}_\alpha}, \quad (2)$$

where $\alpha \in [1, N_p]$ is the phase index, S_α , \mathcal{K}_{r_α} and μ_α are phase saturation, relative permeability and viscosity, respectively. The quantity $\underline{\underline{\sigma}}_\alpha$ represents the transmissibility of the phase. The vector \mathbf{u}_α is the saturation-weighted Darcy velocity and the vector \mathbf{s}_{u_α} is a source, containing terms such as gravity forces and capillary pressure, associated with the force balance. Here \mathbf{K} is

the medium absolute permeability tensor, ϕ is the rock porosity and p is the pressure, assumed independent of phase. The mass source term s_{cty_α} may for example be used to model the exchange of saturation between phases.

The overlapping control volume finite element method discretisation was introduced in part I of this paper ([Gomes et al., 2013](#)). Pressure is represented by finite element basis functions on a given FE mesh partition, with the absolute permeability tensor assumed element-wise constant on the same mesh. Saturation is represented by flat functions on the node-centred CV space dual to the finite element mesh. Velocities are represented by finite element basis functions with support on the spaces formed by the intersection between the saturation CV's and pressure FE's.

The weak form discretised force balance equations for time level n and phase α are thus of the form:

$$\int_{\Omega} Q_i \left(\underline{\underline{\sigma}}_\alpha^n \mathbf{u}_\alpha^n + \nabla p^n - \mathbf{s}_{u_\alpha}^n \right) dV + \oint_{\Gamma_E} Q_i \mathbf{n} (p^n - \tilde{p}^n) d\Gamma + \oint_{\Gamma_{\Omega_p}} Q_i \mathbf{n} (p^n - p_{bc}^n) d\Gamma = \mathbf{0}, \quad (3)$$

where the finite element pressure and velocity fields are given by:

$$p^n := p(\mathbf{r}, t) = \sum_{j=1}^{\mathcal{N}_p} P_j(\mathbf{r}) p_j^n \quad \text{and} \quad \mathbf{u}_\alpha^n := \mathbf{u}(\mathbf{r}, t) = \sum_{j=1}^{\mathcal{N}_u} Q_j(\mathbf{r}) \mathbf{u}_{\alpha,j}^n,$$

in which \mathbf{n} is the normal to the element, \mathcal{N}_p and \mathcal{N}_u are the number of degrees of freedom for the FE pressure and velocity representations, respectively. Here Ω is the volume domain with Ω_E the subspace associated with velocity element E , Γ_E is the interior surface boundary of the element E and Γ_{Ω_p} is the boundary of the domain on which pressure is set weakly to p_{bc} . The inter-element pressure, defined by:

$$\tilde{p} = \lim_{\delta \rightarrow 0} (p(\mathbf{r} + \delta \mathbf{n}) + p(\mathbf{r} - \delta \mathbf{n})) / 2$$

is the average of the finite element pressures on either side of the boundary of element E .

The saturation equations (Eqn. 2) are discretised in space by testing them with CV basis functions and in time with the θ -method, in which $\theta = 0.5$ is

used as much as possible as discussed in part I of this paper. The resulting equations for time step size Δt and phase α are given by:

$$\int_{\Omega} M_i \left(\frac{S_{\alpha,i}^{n+1} - S_{\alpha,i}^n}{\Delta t} \right) dV + \oint_{\Gamma_{CV_i}} (\theta \mathbf{n} \cdot \mathbf{u}_{\alpha}^{n+1} S_{\alpha}^{n+1} + (1-\theta) \mathbf{n} \cdot \mathbf{u}_{\alpha}^n S_{\alpha}^n) d\Gamma - \int_{\Omega} M_i s_{cty,\alpha}^{n+\theta} dV = 0, \quad (4)$$

where $S_{\alpha,j}^n := S(\mathbf{r}, t) = \sum_{j=1}^{N_p} M_j(\mathbf{r}) S_{\alpha,j}^n$. The system is closed by the conservation constraint, $\sum_{\alpha} S_{\alpha} = 1$. A set of coupled equations for pressure and velocity are obtained from the overlapping CVFEM-based discretised Darcy equations (Eqn. 3) and by the sum, over all phases, of the CV-based saturation equations (Eqn. 4).

3. Classical Buckley-Leverett Test-Cases

In this section, the Buckley-Leverett (Buckley and Leverett, 1942) problem is modelled with phase 1 ($S_l = 1$) being injected at a constant velocity $u_1 = 1$ into a porous medium saturated by phase 2 ($S_2 = 1, \phi = 0.5$).

Relative permeability in this paper is calculated as a quadratic function of saturation with residual saturation of phase 1 and 2 $S_1 = 0.1$ and $S_2 = 0.3$, respectively. The endpoint of the relative permeabilities of phases 1 and 2 are 0.8 and 0.3, respectively (see Table 1).

The length of the domain is 4 non-dimensional units. On the outlet boundary condition, the pressure level is set to zero and all remaining boundary conditions are weakly applied.

Despite the one-dimensional nature of the problem, 2- and 3-D simulations were performed using structured and unstructured meshes to evaluate the multi-dimensional capabilities of the model.

All simulations used the overlapping mixed-DGFEM with P_0DG-P_1 , P_1DG-P_2 and/or P_2DG-P_3 element-pairs with continuous / discontinuous (between elements) formulations with saturation collocated at pressure nodes. Although saturation is calculated using a CV formulation, a FEM interpolation is used to form the high-order fluxes and these are also used for most of the plots. In all 1-D simulations, mesh grids were designed with equisized elements, whilst 2-D meshes were regular, structured and one-element wide with unity aspect ratio. The width of the 2-D numerical domain is inversely proportional to the number of elements. The time-step size varied

linearly within $0.125\text{-}3.125 \times 10^{-3}$ seconds range for 1-D simulations, and a fixed time-step of 1.0×10^{-4} for all 2- and 3-D simulations.

Convergence Analysis. Convergence analyses were performed for the 1- and 2-D problems with a number of (regular) mesh resolution and element pairs. The time-step size was linearly varied from 1.25×10^{-4} to 3.25×10^{-3} seconds. Figure 1 shows phase 1 saturation profiles at time $t = 0.5$ for mesh grids varying from 5 to 500 elements, and for different element types – P_0DG-P_1 , P_1DG-P_2 and P_2DG-P_3 (the geometry symmetry line is used to extract data from the 2-D simulations). In general, results are in good agreement with the analytic solution for all resolutions and element-pairs however, for coarser meshes, high-order elements-pairs (P_2DG-P_3 for 1-D using 5 elements and P_1DG-P_2 for 2-D using 20 elements) perform significantly better and are able to capture the sharp-front more accurately. As far as the 2-D simulations are concerned, the coarse mesh simulation performs slightly worse than its 1-D counterpart but for higher resolutions, results are identical.

These conclusions become clearer in Fig. 2, where convergence rates are shown. The L1 and L2 errors are defined as,

$$\frac{\sum_{i=1}^N |S_i^{\text{simulated}} - S_i^{\text{analytical}}|}{N} \quad \text{and} \quad \sqrt{\frac{\sum_{i=1}^N (S_i^{\text{simulated}} - S_i^{\text{analytical}})^2}{N}},$$

respectively, where S_i is the saturation of phase 1 at the i -th node point. In addition, convergence rates for simulations performed with full upwinding scheme are shown.

3.1. Discontinuous Formulation

In this section, results for the fully discontinuous formulation are presented. Discontinuity of the pressure field between elements allows the use of coarse meshes to represent abrupt changes in the solution. Figure 4 shows converged CV phase 1 saturation solutions and the corresponding FEM interpolated solutions. This solution was obtained with upwinding within and between the elements. Convergence rates for the test-cases performed with the fully discontinuous formulation (between elements) are shown in Fig. 5.

Solutions obtained with upwinding and central difference schemes are shown in Fig. 6 for different resolutions, and compared against the continuous (converged) solution with good agreement. In this plot, one can also note the suppression of oscillations resulting from the upwinding scheme.

In Figure 7, saturation solutions obtained using first (P_1) and second-order (P_2) functions in the FE representation of pressure are shown both for continuous and discontinuous representations. At coarse resolution the discontinuous solution is more accurate. By comparing P_1 and P_2 solutions in pressure, we demonstrate that near the shock-front there is little benefit in using high-order discontinuous elements, thus linear elements perform well compared to quadratic elements.

3.2. 2- and 3-D Simulations

Following the convergence analysis, a number of numerical experiments were performed to assess the robustness of the method in fully unstructured meshes. Phase 1 saturation surface maps (and the corresponding meshes) for 2- and 3-D simulations at time $t = 0.5$ are shown in Fig. 8. The simulations presented in this section were performed using the P_1 DG- P_2 element-pair in fully unstructured mesh-grid.

Saturation profiles for the phase 1 at time $t = 0.5$ are shown in Fig. 9. Results are not spatially averaged and the geometry symmetry line is used to extract data for all simulations. The structured coarse mesh uses 1×19 layers in the lateral and flow directions, respectively. The structured medium mesh uses 3×40 layers. The solution field converged towards the analytical solution with the increase of the mesh resolution; additionally, no substantial improvement was observed when structured and unstructured P_1 DG- P_2 mesh were used. However, the use of unstructured mesh (and potentially higher-order triangle and tetrahedra elements) is advantageous for flow simulation in complex geometries as demonstrated by Jackson et al. (2013).

4. Immiscible Displacement in Heterogeneous Porous Media

This test case was designed to demonstrate the numerical robustness of the method when solving multi-fluid flow problems involving heterogeneous porous media. Here, phase 1 is injected in a fully saturated ($S_2 = 1$) 2-D square porous matrix domain of side length one and uniform porosity ($\phi = 0.5$) – Fig. 10. However, unlike the test-cases in Section 3, the permeability field is not uniform and four equally sized ‘regions’ are designed. Permeability fields in regions R1 and R4 are 4 times larger than that of regions R2 and R3, i.e.,

$$\mathbf{K}^{(1)} = \mathbf{K}^{(4)} = 4\mathbf{K}^{(2)} = 4\mathbf{K}^{(3)}.$$

Phase 1 is uniformly injected at a velocity of $u_l = 1$ on the left boundary to displace the oil in the porous domain. On the outflow boundary the pressure level is set to zero. Free-slip boundary conditions are applied on the sides of the domain for the two velocity fields. All boundary conditions are applied weakly. For relative permeability calculations (\mathcal{K}_{rk}), the irreducible phase 1 and residual phase 2 saturations are set to 0.1 and 0.2, respectively; the endpoint of phase 2 and phase 1 relative permeabilities are 0.3 and 0.8, while the Corey exponent is assumed as 2.

Two sets of simulations are performed using coarse (402 elements with 2412 nodes) and fine (3714 elements with 22284 nodes) meshes; in the first set (A) the overlapping mixed DGFEM and the P_1 DG- P_2 element-pairs are used, with time-step sizes of 1×10^{-3} and 5×10^{-4} seconds for simulations performed with coarse and fine meshes, respectively. In the second set of experiments (B) P_2 DG- P_2 DG element-pairs are used, with time-step sizes of 5×10^{-4} and 1×10^{-4} seconds for coarse and fine meshes.

Figure 11 shows the phase 1 saturation profile maps (at time $t = 0.08$ seconds) for all four simulations. The results yielded by the experiment (A) are depicted in the top left, coarse mesh, and top right, fine mesh. The results obtained from experiment (B) located on the bottom left, coarse mesh, and bottom right, fine mesh. A laboratory experiment with similar setup was performed by [Dawe and Grattoni \(2008\)](#) to investigate miscible and immiscible displacement in heterogeneous permeability and wettability cases.

For the immiscible displacement, phase 1 was uniformly injected from the left-hand side boundary (injection rate of ~ 1 ml/min in a domain of $20 \times 10 \times 0.6$ cm, glass ballotini beads produced porosity of 0.4, and permeability ratio of 2.5). Snapshots in Fig. 11 show the phase 1 flood ‘fingering’ across the central regions ($R1 \Rightarrow R4$) demonstrating the preferential flow through highly permeable matrix. This is in good qualitative agreement with the laboratory experiments (see Figs. 5 and 6 in [Dawe and Grattoni, 2008](#)).

Figure 12 shows phase 1 saturation profiles (at time $t = 0.08$ seconds) for all simulations. Comparing the results obtained by both sets of experiments, a better agreement between the results yielded by the simulations (B) – i.e., with P_2 DG- P_2 DG element-pairs, can also be observed.

5. Underground Caisson

Numerical models may fail when a high permeability gradient is in the domain by introducing fluid in the low-permeability region not due to a physical phenomena, but because of numerical dispersion. Thus, the purpose of this numerical experiment is to test the fluid flow behaviour across two distinct porous media characterised by high different permeabilities.

The considered domain is characterised by a low-permeability square region, with dimensions of 0.5×0.5 unit-area, which is embedded in a high-permeability region with dimension 1×1 . The porosity of the whole domain and the permeability of the high-permeability region are of 0.5 and 10^4 respectively. The necessary parameters to obtain the relative permeability (\mathcal{K}_{rk}) are the following: the irreducible phase 1 and residual phase 2 saturations are $S_{wi} = 0.1$ and $S_{orw} = 0.3$, respectively; Corey exponent is $N = 2$; the endpoint of phase 2 and phase 1 relative permeabilities are 0.3 and 0.8.

Regarding the initial state and the boundary conditions of the experiment, at rest state the domain is fully saturated of phase 2 ($S_o = 1$). Next, phase 1 is injected with a constant velocity of $(1, 0)$ through the left boundary that can exit only through the right boundary, which have a constant pressure of zero.

Two sets of numerical experiments are performed, one uses the P_0DG-P_1 element pair and a time step of 5×10^{-3} and the second experiment the P_1DG-P_1DG element-pair and a time step of 1×10^{-4} . Both use the same mesh and the same permeability map, see Fig. 13 (top).

Figure 13 displays snapshots of phase 1 saturation profile at $t = 0.15$ and $t = 0.5$ for both simulations. The simulation performed with P_0DG-P_1 elements presents a small dispersion of phase 1 into the low-permeability region, whereas the saturation profile in the P_1DG-P_1DG simulation presents a defined frontier between the low-permeability region and the high-permeability area. Despite this small difference, both experiments are in good agreement and provide satisfactory results by making the fluid to go around the low-permeability region.

6. High-Permeability Wedge-Shaped Region

Fractures and cracks in porous media are ubiquitous, however, they are not easy to model due to their small size. However, cracks may have a dramatic impact in the behaviour of the flow since they can act as conductors with

a very high permeability. Usually, they are characterised by thin tip and a high permeability. In order to test the behaviour of the model presented in this paper, in the present numerical experiment consists in a wedge-shaped high-permeability region embedded in a rectangular low-permeability (permeability ratio of 100) domain. The permeability map is shown in Fig. 14.

Three different experiments were performed, two using the P_0 DG- P_1 element-pair and one using the P_2 DG- P_1 DG element-pair. For the first experiment using the P_0 DG- P_1 element-pair, the mesh is composed of 56902 elements, whereas for the second experiment the mesh is composed of 672 elements. For the P_2 DG- P_1 DG element-pair example this latter mesh is considered as well. The non-dimensional rectangular domain is 1×0.1 and the wedge is defined by a height of 0.025 and a slope of $1/30$. The porosity is uniform and equal to 0.5. The irreducible water and residual oil saturations are set to zero. Initially, the porous media is fully saturated with an incompressible fluid ($S_2 = 1$). An immiscible fluid is injected from the left boundary with a constant pressure of 1 and a saturation of $S_1 = 1$. On the outflow boundary, the pressure level is set to zero.

Free-slip boundary conditions are applied on the sides of the domain for the two velocity fields. All remaining boundary conditions are applied weakly. The irreducible water and residual oil saturation are both set to zero. The time steps considered are 1×10^{-3} and 1×10^{-5} for the P_0 DG- P_1 and P_2 DG- P_1 DG element-pair experiments, respectively.

The saturation pictures displayed in Fig. 14 shows the water-phase saturation maps at times $t = 0.011$ and $t = 0.014$. The three test-cases handle this benchmark adequately by introducing the majority of the input flow through the high permeability area. However, as in the previous section, the P_0 DG- P_1 -based numerical experiment presents a dispersion of the water-phase in the vicinity of the wedge. Moreover, in the experiment with fewer elements the effect of the dispersion affects the behaviour of the fluid dramatically. It can be seen how the front of the water phase is delayed compared with the other two experiments. On the other hand, the P_2 DG- P_1 DG simulation presents a well-defined boundary of the water-phase within the wedge.

7. High-permeability canals

In this section we deal with a hexahedral domain with two canals inside that are characterised by a higher permeability. Thus, three regions with different permeabilities are considered. The domain, the permeability map

and the mesh (composed of 201892 tetrahedra) are displayed in Fig. 15. For the numerical experiment we have considered a homogeneous porosity $\phi = 0.25$; the irreducible water and residual oil saturations are set to 0.2 and 0.2.

Initially, the domain is filled with a mixture of movable oil and immovable water, $S_o = 0.8$ and $S_w = 0.2$ respectively. Next, water is injected into the domain through one face at constant pressure. All boundaries are considered as barriers to flow except one inlet face and one outlet face with an input pressure of 10^6 and an outlet pressure of 0 respectively. These pressure boundary conditions are applied weakly.

The simulations were performed using the P_0DG-P_1 element-pair. The results for 7.9 years and an internal slice in 2-D are depicted in Fig. 15. As expected the majority of the flow goes through the high permeability canals.

8. Conclusions

This article is the second in a series of papers describing a new CVFEM formulation for multi-fluid flows in porous media. In the first paper, we described the new model which is based upon two computational building blocks: (a) consistent pressure-velocity formulation in a dual mesh-spaces that led to the new overlapping control volume, continuous and discontinuous between finite elements (OCVFEM), and (b) a new family of triangular/tetrahedral element types. The novel formulation, although generic in nature (thus not restricted to porous media applications as demonstrated by Pavlidis et al., 2013b,a, for interface tracking problems), has demonstrated numerical robustness and accuracy in multi-fluid subsurface flow problems.

The focus of this paper is two-fold: to demonstrate the model accuracy in multi-fluids subsurface flows and, to exploit the new formulation to solve problems involving highly heterogeneous porous media.

The classical Buckley-Leverett problem was used to assess model convergence, accuracy and performance of the upwind formulation. We demonstrated that the solutions obtained from the model summarised here (see Gomes et al., 2013, for a full description) are in good agreement with analytical solutions even if a (relatively) coarse resolution and low-order accuracy element-pairs are used. Saturation profiles obtained from the fully discontinuous formulation was successfully compared against the continuous-based solutions with a lower grid resolution.

In order to assess the performance of the formulation for heterogeneities in permeability field across the porous matrix, we successfully compared the flood behaviour of the numerical solution against laboratory experiments. Additional tests involving high-permeability ratios, skewed elements, low- and high-order element-pairs and unstructured mesh were performed to assess the accuracy and performance of the upwind velocity / permeability formulation.

Overall, in these two initial papers we demonstrated the flexibility and numerical accuracy of the new multi-phase flow model formulation. The model was successfully validated against: (a) analytical solutions for advection-diffusion equations and (b) classical Buckley-Leverett problem. The flow behaviour in subsurface water-flood conditions was qualitatively validated against lab-scale experiments. Further validation tests will need to be performed to rigorously assess the permeability and wettability effects in gravity-driven subsurface flows.

Acknowledgements

Dr D. Pavlidis would like to acknowledge the support from the following research grants: EPSRC ('Computational Modelling for Advanced Nuclear Power Plants') and EU/FP7 ('Thermo-Hydraulics for Innovative Nuclear Systems' – THINS). Funding for Dr P. Salinas from the Qatar Carbonates and Carbon Storage Research Centre (QCCSRC), provided jointly by Qatar Petroleum, Shell and the Qatar Science and Technology Park, is gratefully acknowledged. Dr Z. Xie is supported by EPSRC ('Multi-Scale Exploration of Multi-phase Physics in Flows' – MEMPHIS). Part funding for Profs. Jackson and Muggeridge under the TOTAL Chairs programme at Imperial College is also acknowledged.

References

- Buckley, S., Leverett, M., 1942. Mechanism of fluid displacement in sands. Trans. AIME 146 (107), 1–7.
- Dawe, R., Grattoni, C., 2008. Experimental displacement patterns in a 2×2 quadrant block with permeability and wettability heterogeneities – problems for numerical modelling. Transp. Porous Med. 71, 5–22.

Gomes, J., Pavlidis, D., Percival, J., Mostaghimi, P., Salinas, P., Xie, Z., Pain, C., Jackson, M., Blunt, M., 2013. The overlapping control volume finite element method for multi-fluids porous media flow modelling. Part I: Formulation. *Computer Methods in Applied Mechanics and Engineering* (Submitted).

Jackson, M., Gomes, J., Mostaghimi, P., Percival, J., Tollit, B., Pavlidis, D., Pain, C., El-Sheikh, A., Muggeridge, A., Blunt, M., 2013. Reservoir modeling for flow simulation using surfaces, adaptive unstructured meshes, and control-volume-finite-element methods. In: *SPE Reservoir Simulation Symposium*. Texas, USA.

Pavlidis, D., Gomes, J., Pain, C., Matar, O., 2013a. Interface-tracking using a compressive advection method and a compositional modelling approach. In: *Proceedings of the 2013 International Conference on Multiphase Flow – ICMF 2013*. Jeju, South Korea.

Pavlidis, D., Gomes, J., Xie, Z., Percival, J., Pain, C., Matar, O., 2013b. Compressive-advection and multi-component methods for interface-capturing. *Journal of Computational Physics* (Submitted).

List of Figures

1	Buckley-Leverett test-cases: 1-D Saturation profiles for a number of element pairs and grid resolutions – P_0DG-P_1 (top), P_1DG-P_2 , P_2DG-P_3 (bottom).	15
2	Buckley-Leverett test-cases: L1 (top) and L2 (bottom) error convergence rates for a number of (continuous) element pairs.	16
3	Buckley-Leverett test-cases: Comparison of the optimal upwind formulation when using upwinding (OU) and coupled upwind/downwind (OU-D). The finite element interpolation of the saturation field (S_1) is shown at different mesh resolutions. Downwind seems to detract from the accuracy of the solution.	17
4	Buckley-Leverett test-cases: Two element solution using the discontinuous formulation. Saturation field from both CV solution and FEM interpolation are shown.	18
5	Buckley-Leverett test-cases: L1 (top) and L2 (bottom) error convergence rates for a number of fully discontinuous (between elements) element pairs.	19
6	Buckley-Leverett test-cases: Saturation field obtained from the discontinuous and continuous formulation with different mesh resolutions. Solutions with (top) and without (bottom) upwinding scheme. Notice that oscillations are suppressed with the upwinding scheme.	20
7	Buckley-Leverett test-cases: Saturation field obtained from (top) continuous and discontinuous (between elements) formulations (solution with 50 elements may be considered as a converged result). Solution obtained (bottom) from linear pressure (P_1) formulation with different mesh resolution with comparison against P_2 -pressure formulation (continuous).	21
8	Buckley-Leverett test-cases: phase 1 saturation surface maps for a 2- (770 triangles) and 3-D (1207 tetrahedra) simulations (P_1DG-P_2 unstructured mesh grids) at time $t = 0.5$	22
9	Buckley-Leverett test-cases: 2- and 3-D phase 1 saturation profiles with P_1DG-P_2 elements. Sensitivity analysis for (top) grid resolution using structured P_1DG-P_2 mesh, and (bottom) mesh type.	23

10	Heterogeneous permeability test-cases: schematic including boundary conditions. Darker areas (R1 and R4) represent regions with high permeability.	24
11	Heterogeneous permeability test-cases: phase 1 saturation maps at time $t = 0.08$ seconds. Upper- and lower-rows show saturation fronts (superimposed with unstructured mesh) calculated with P_1DG-P_2 and P_2DG-P_2DG elements, respectively. Left/Right columns: 402 triangles (2412 nodes) and 3714 triangles (22284 nodes) meshes.	25
12	Heterogeneous permeability test-cases: phase 1 saturation profiles at time $t = 0.08$ seconds. Top left: profiles at the diagonal starting at the bottom left corner of the domain. Top right: profiles at the diagonal starting at the top left corner of the domain. Bottom left: profiles at $x = 0.4$. Bottom right: profiles at $y = 0.4$	26
13	Underground Caisson: Initial configuration of porous matrix consisting of a low-permeability square embedded in a high-permeability region (top). Phase 1 saturation profile at 0.15 (left) and 0.5 seconds (right) within the transient for simulation performed using P_0DG-P_1 (middle) and P_1DG-P_1DG (bottom) element-pairs.	27
14	Wedged-shaped region: (a) two phase flow in a rectangular domain with an internal wedge-shaped region with high-permeability. Snapshots of water-phase saturation profiles of simulations performed with a fine mesh P_0DG-P_1 simulation (top) and course mesh P_0DG-P_1 simulation (middle) and course mesh P_2DG-P_1DG simulation (bottom) at (b) 0.011 and (c) 0.0014 seconds.	28
15	Hexahedron domain: (a) Permeability map and mesh used. Snapshots of water-phase saturation profiles of simulations performed with P_0DG-P_1 (b) 3-D solution and (c) 2-D internal slice.	29

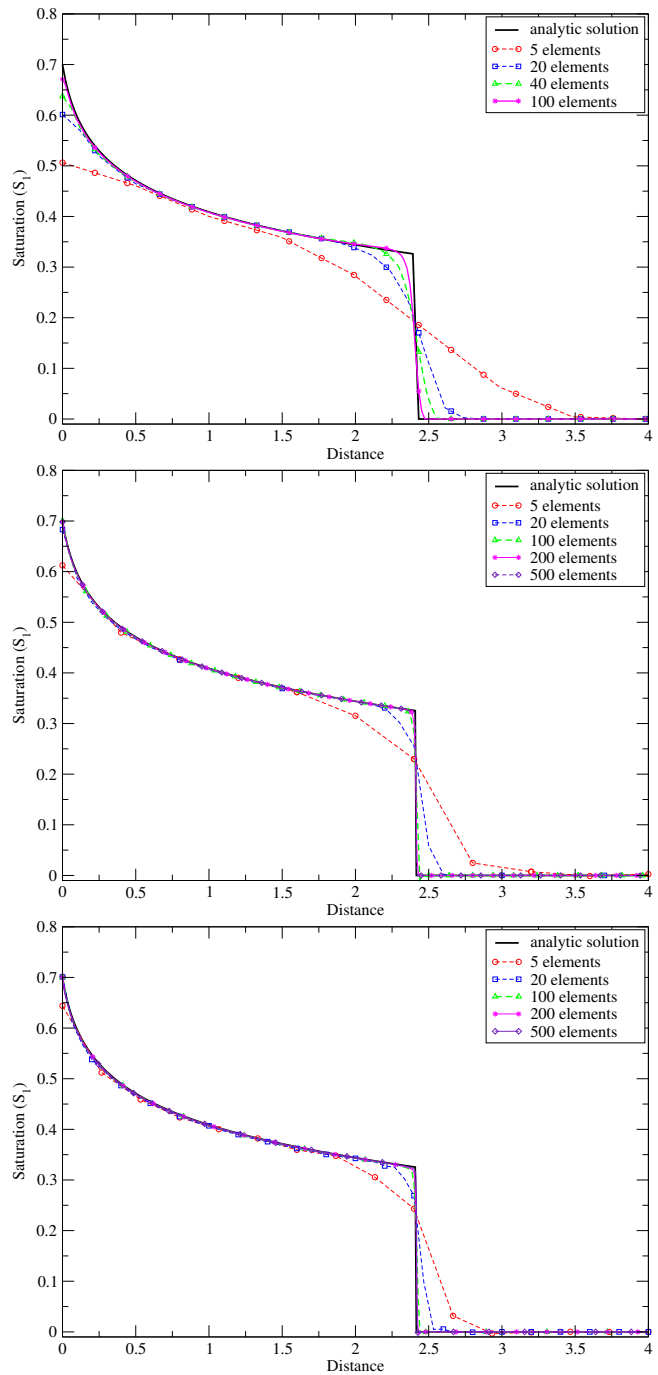


Figure 1: Buckley-Leverett test-cases: 1-D Saturation profiles for a number of element pairs and grid resolutions – P_0DG-P_1 (top), P_1DG-P_2 , P_2DG-P_3 (bottom).

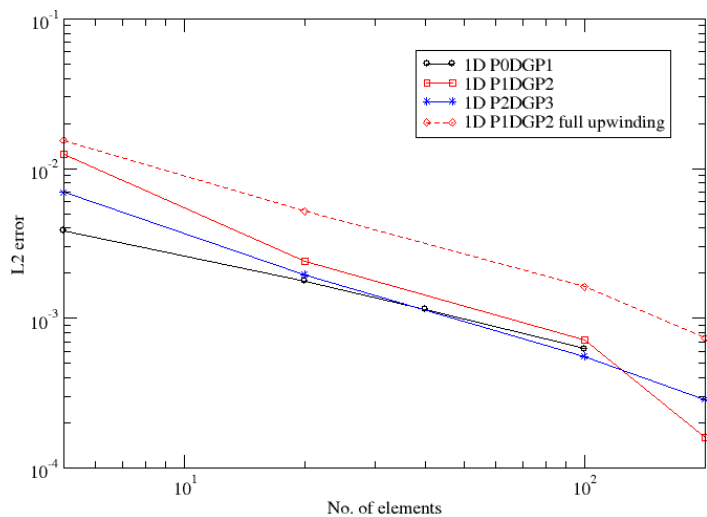
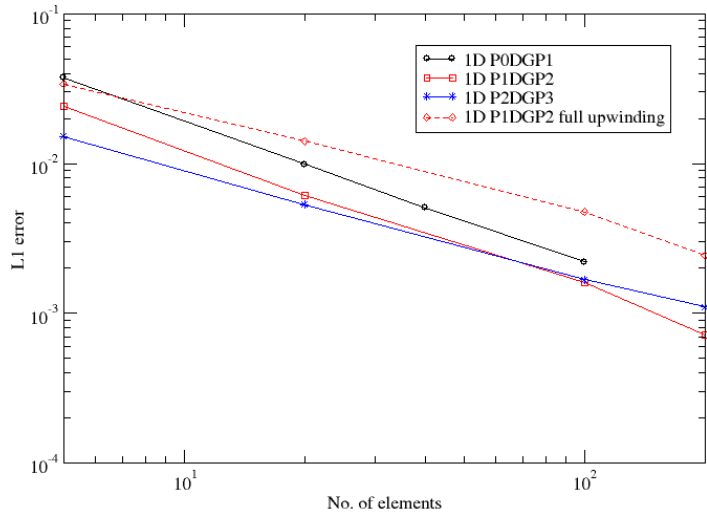


Figure 2: Buckley-Leverett test-cases: L1 (top) and L2 (bottom) error convergence rates for a number of (continuous) element pairs.

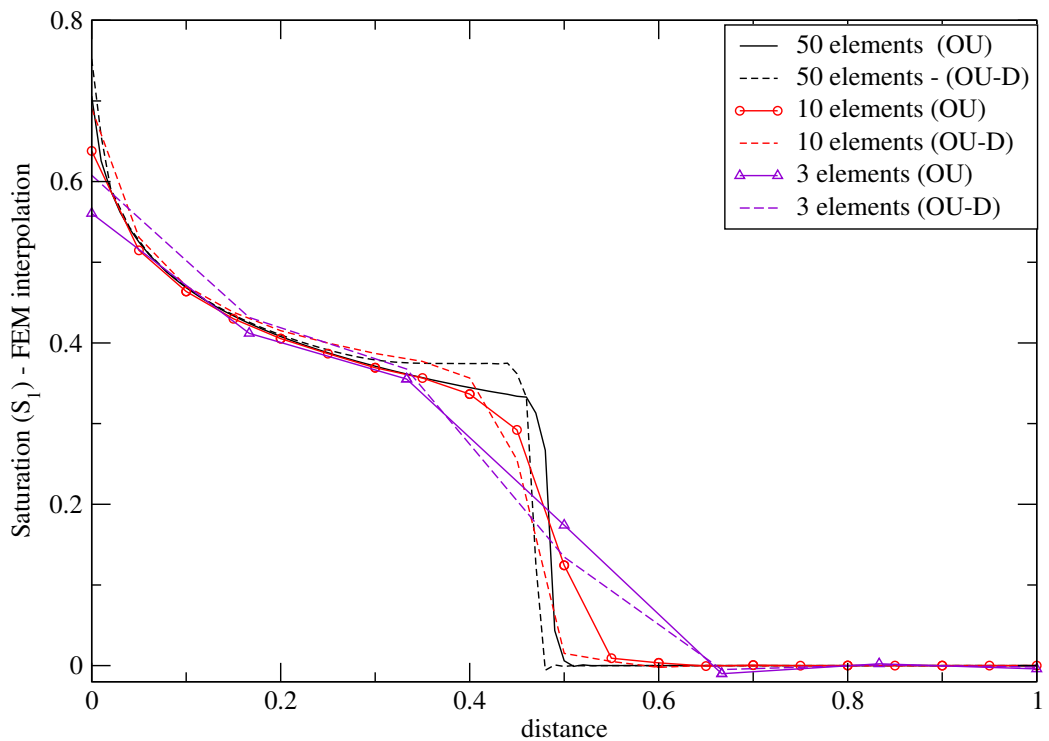


Figure 3: Buckley-Leverett test-cases: Comparison of the optimal upwind formulation when using upwinding (OU) and coupled upwind/downwind (OU-D). The finite element interpolation of the saturation field (S_1) is shown at different mesh resolutions. Downwind seems to detract from the accuracy of the solution.

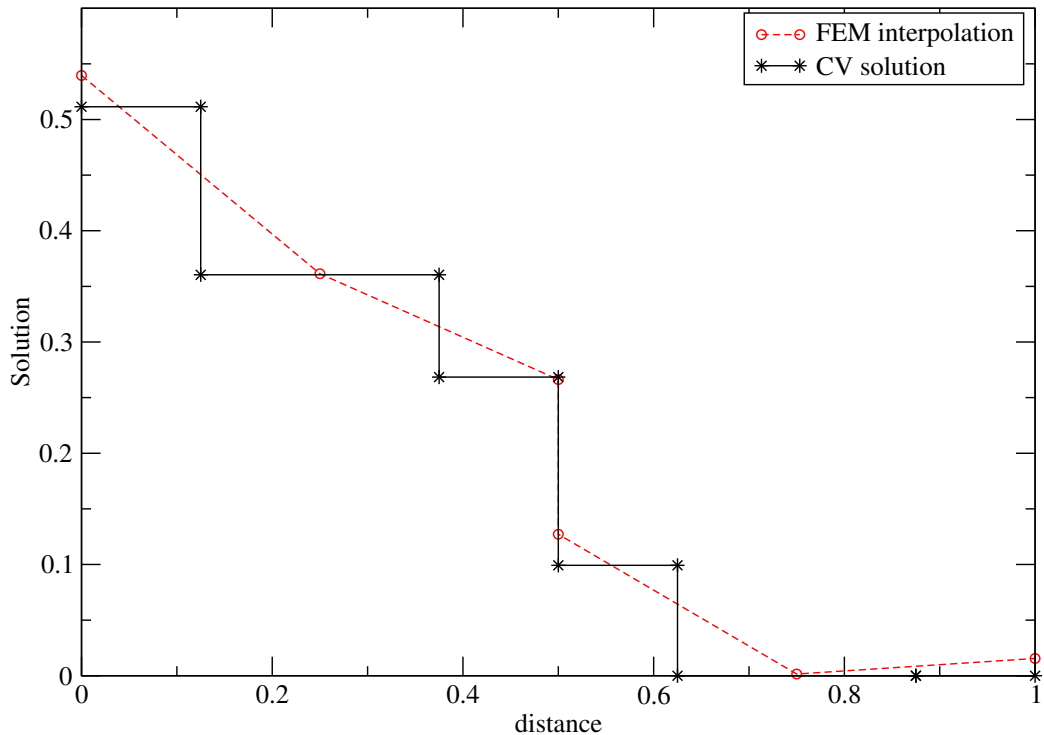


Figure 4: Buckley-Leverett test-cases: Two element solution using the discontinuous formulation. Saturation field from both CV solution and FEM interpolation are shown.

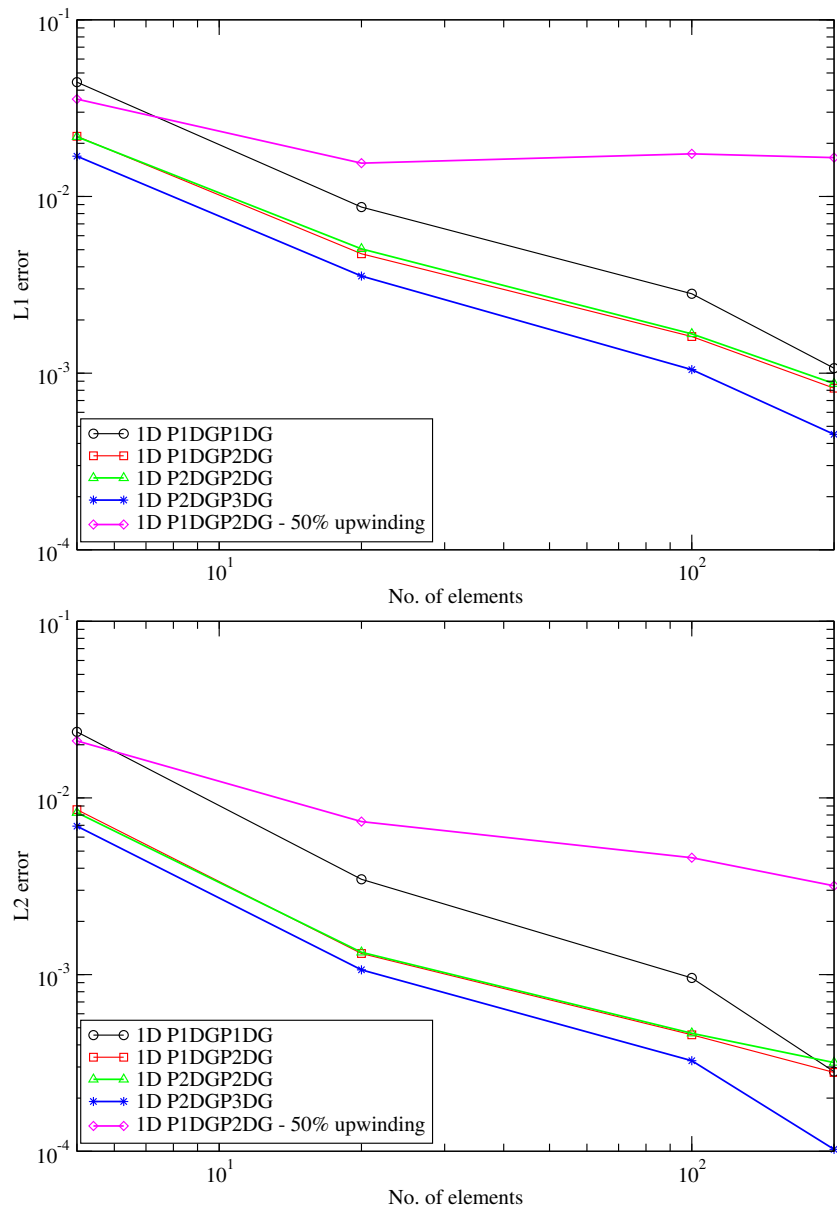


Figure 5: Buckley-Leverett test-cases: L1 (top) and L2 (bottom) error convergence rates for a number of fully discontinuous (between elements) element pairs.

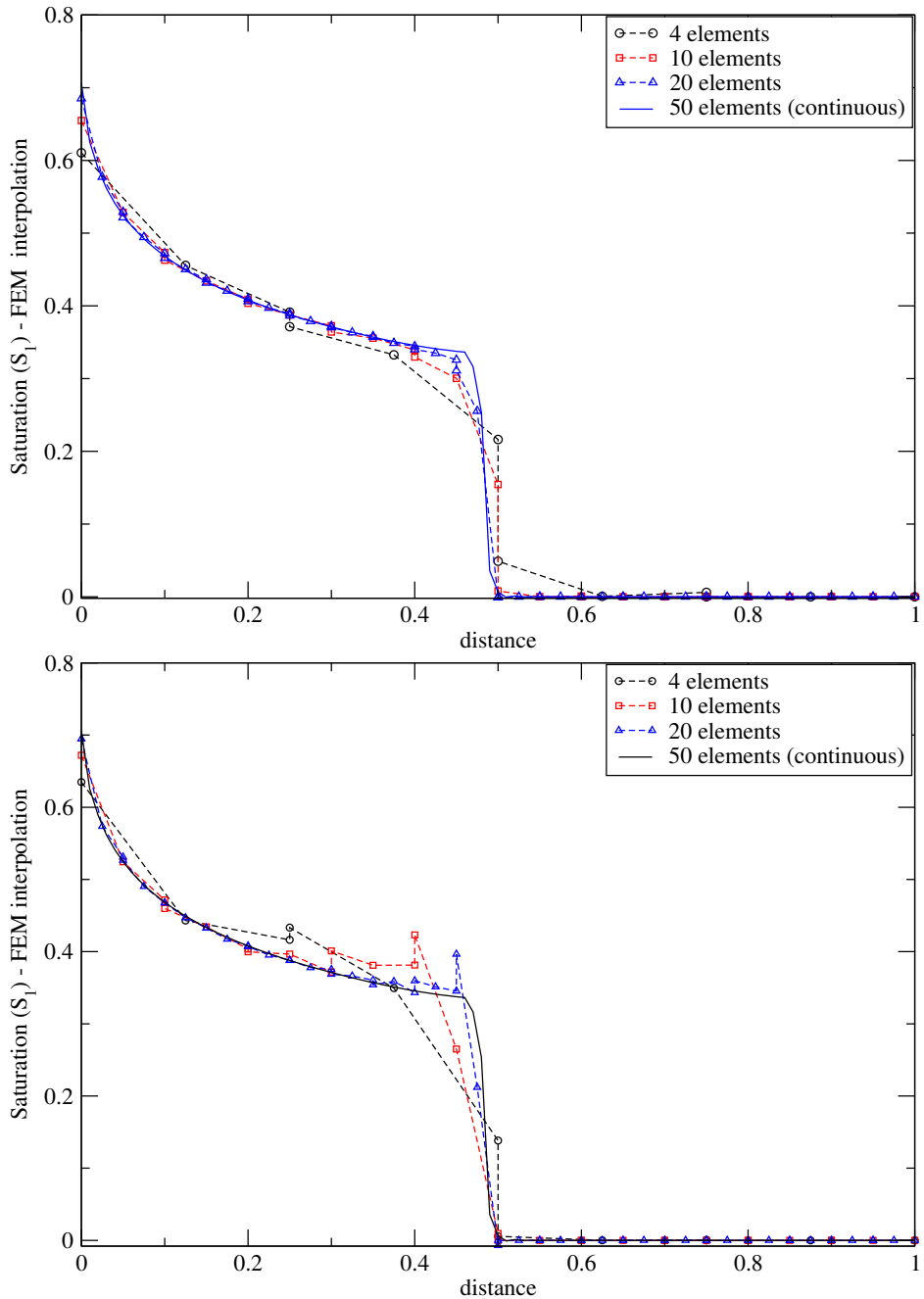


Figure 6: Buckley-Leverett test-cases: Saturation field obtained from the discontinuous and continuous formulation with different mesh resolutions. Solutions with (top) and without (bottom) upwinding scheme. Notice that oscillations are suppressed with the upwinding scheme.

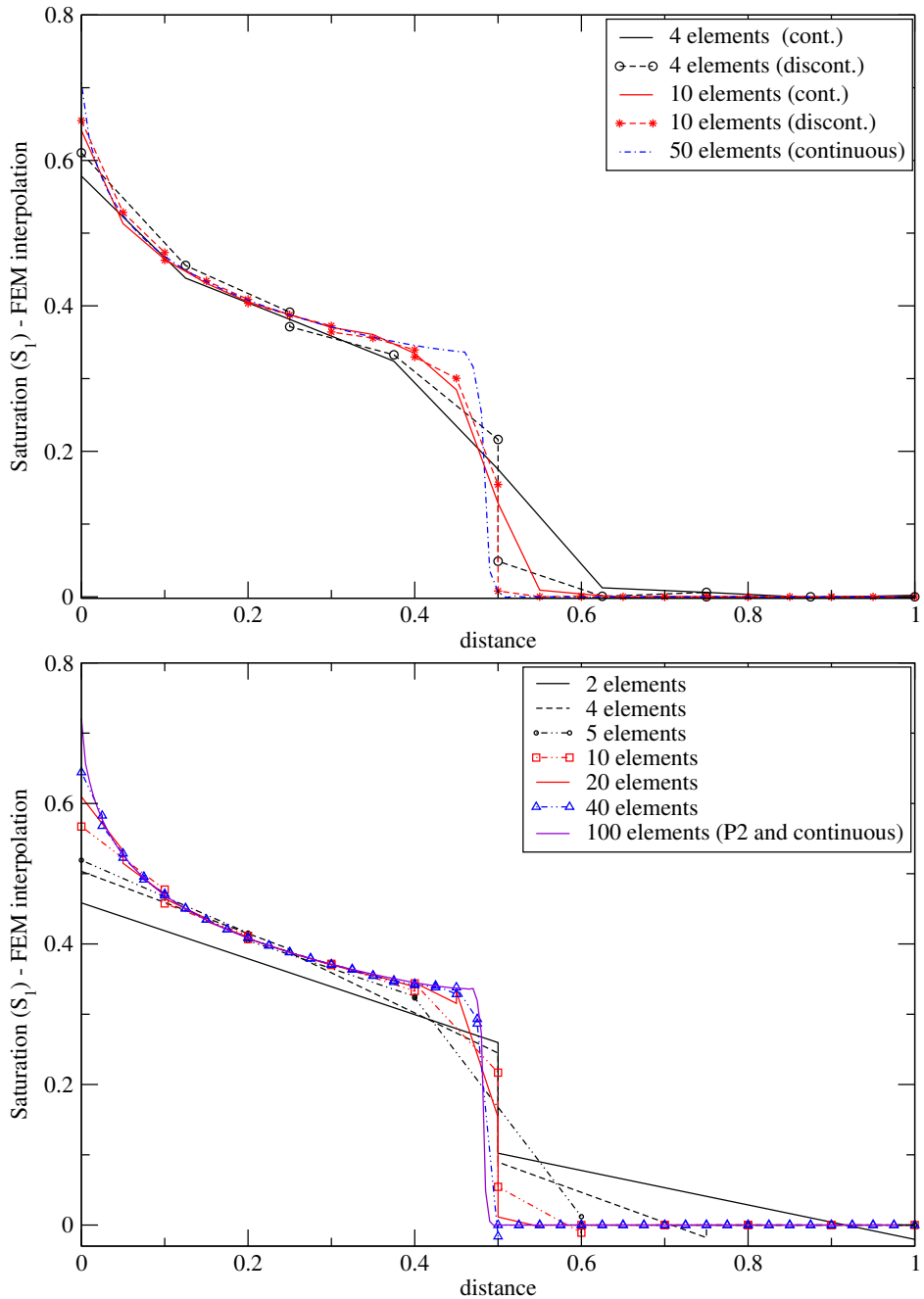


Figure 7: Buckley-Leverett test-cases: Saturation field obtained from (top) continuous and discontinuous (between elements) formulations (solution with 50 elements may be considered as a converged result). Solution obtained (bottom) from linear pressure (P1) formulation with different mesh resolution with comparison against P2-pressure formulation (continuous).

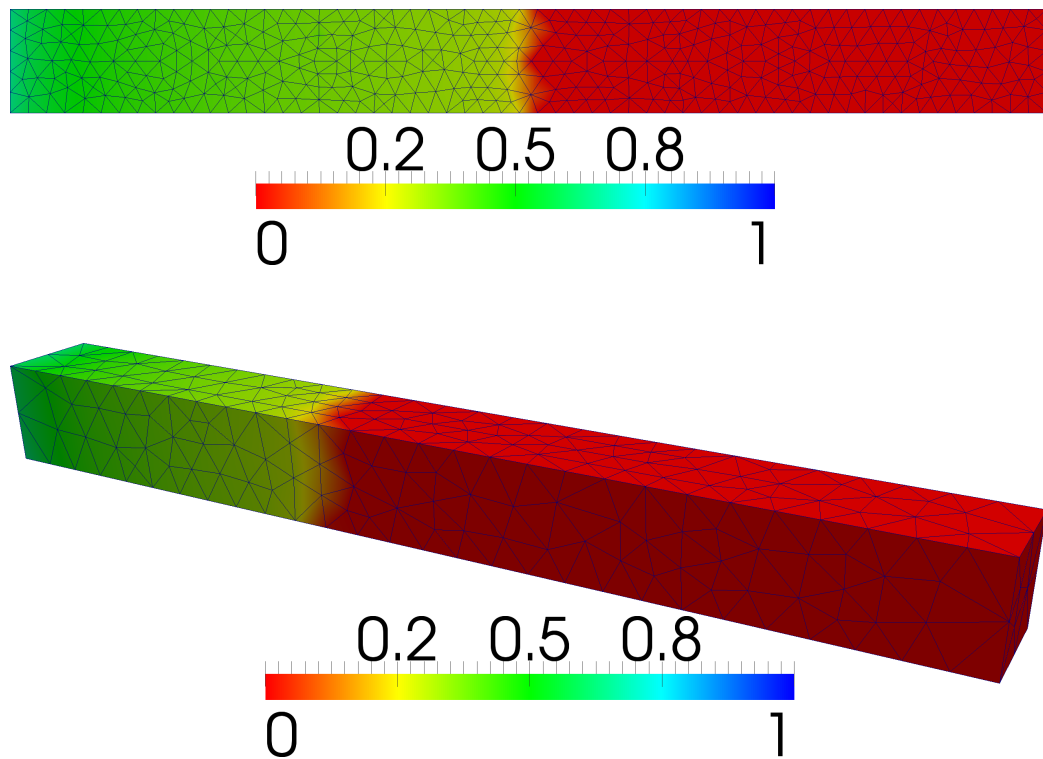


Figure 8: Buckley-Leverett test-cases: phase 1 saturation surface maps for a 2- (770 triangles) and 3-D (1207 tetrahedra) simulations (P_1 DG- P_2 unstructured mesh grids) at time $t = 0.5$.

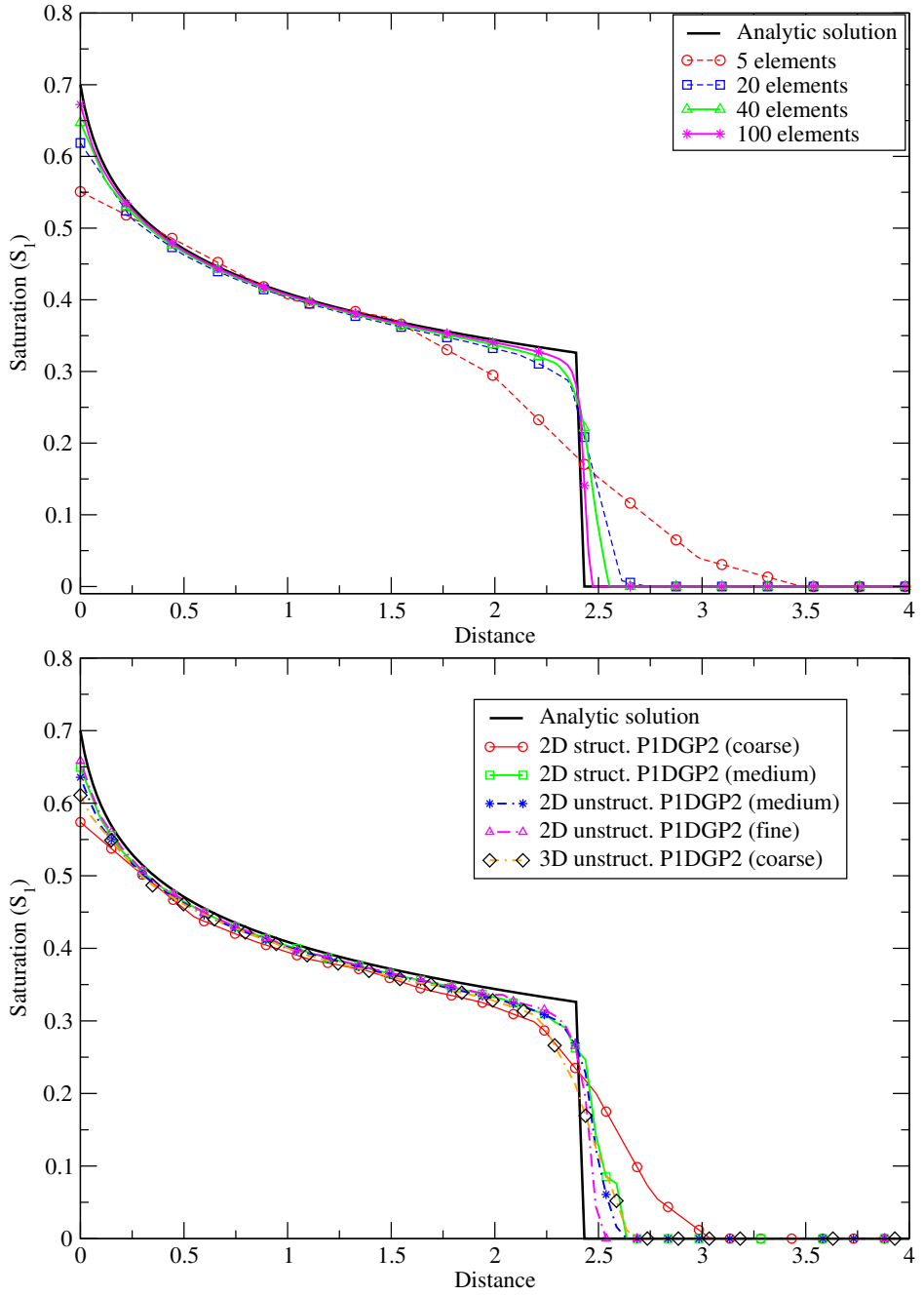


Figure 9: Buckley-Leverett test-cases: 2- and 3-D phase 1 saturation profiles with P_1DG-P_2 elements. Sensitivity analysis for (top) grid resolution using structured P_1DG-P_2 mesh, and (bottom) mesh type.

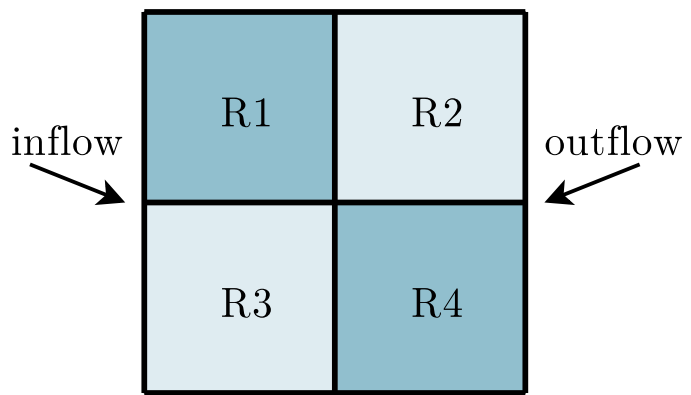


Figure 10: Heterogeneous permeability test-cases: schematic including boundary conditions. Darker areas (R1 and R4) represent regions with high permeability.

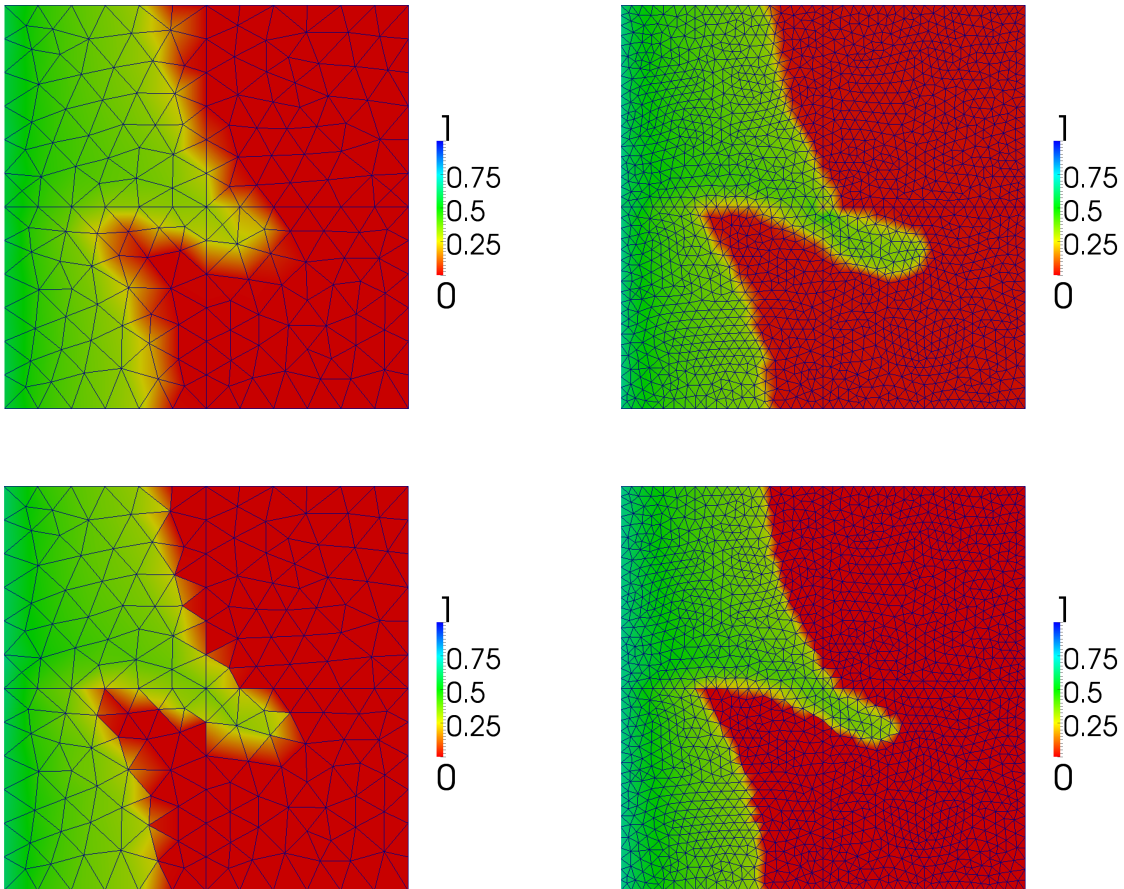


Figure 11: Heterogeneous permeability test-cases: phase 1 saturation maps at time $t = 0.08$ seconds. Upper- and lower-rows show saturation fronts (superimposed with unstructured mesh) calculated with P_1DG-P_2 and P_2DG-P_2DG elements, respectively. Left/Right columns: 402 triangles (2412 nodes) and 3714 triangles (22284 nodes) meshes.

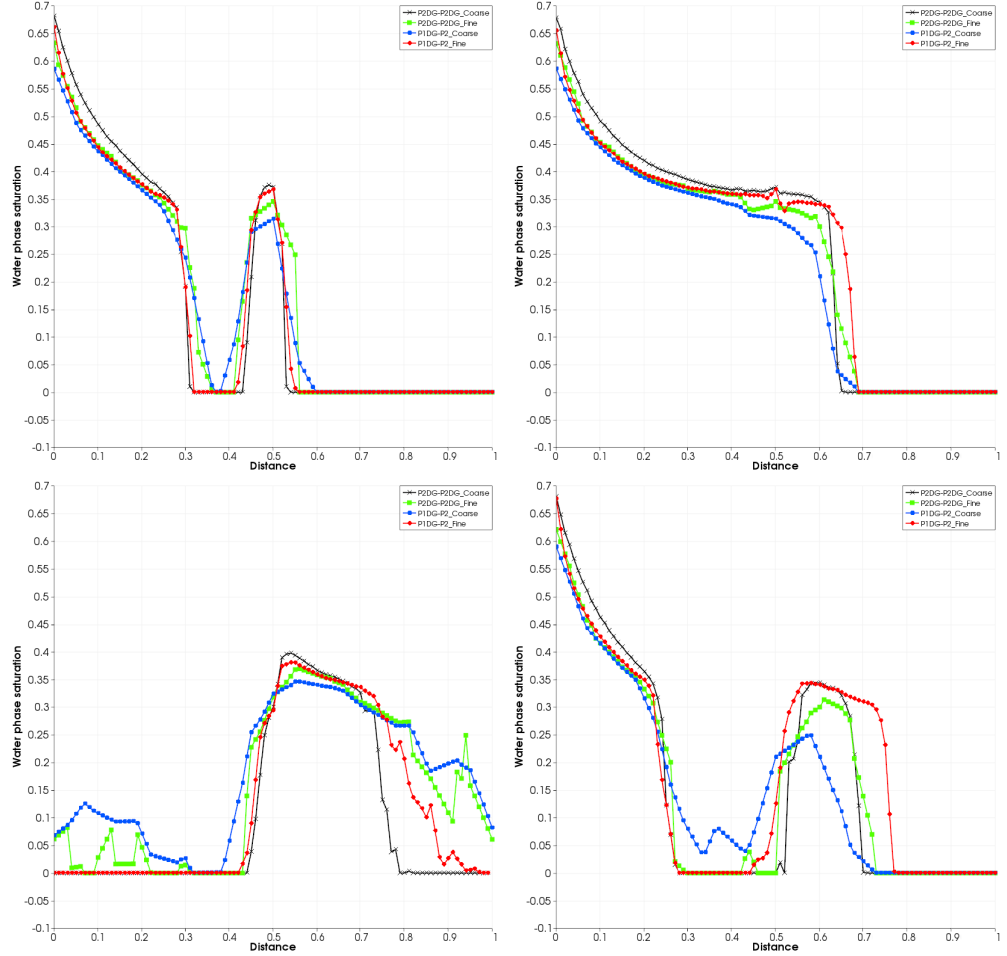


Figure 12: Heterogeneous permeability test-cases: phase 1 saturation profiles at time $t = 0.08$ seconds. Top left: profiles at the diagonal starting at the bottom left corner of the domain. Top right: profiles at the diagonal starting at the top left corner of the domain. Bottom left: profiles at $x = 0.4$. Bottom right: profiles at $y = 0.4$.

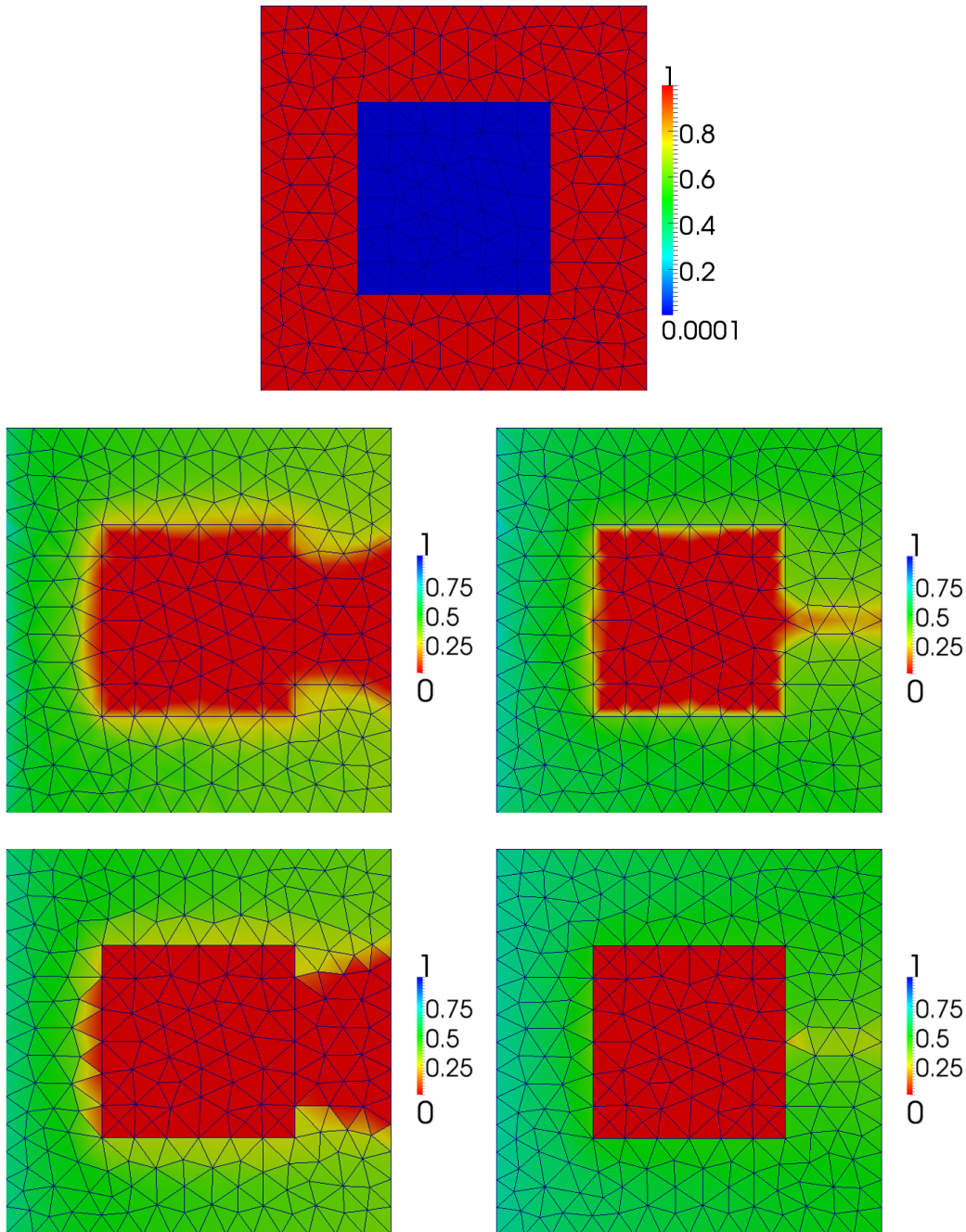


Figure 13: Underground Caisson: Initial configuration of porous matrix consisting of a low-permeability square embedded in a high-permeability region (top). Phase 1 saturation profile at 0.15 (left) and 0.5 seconds (right) within the transient for simulation performed using P₀DG-P₁ (middle) and P₁DG-P₁DG (bottom) element-pairs.

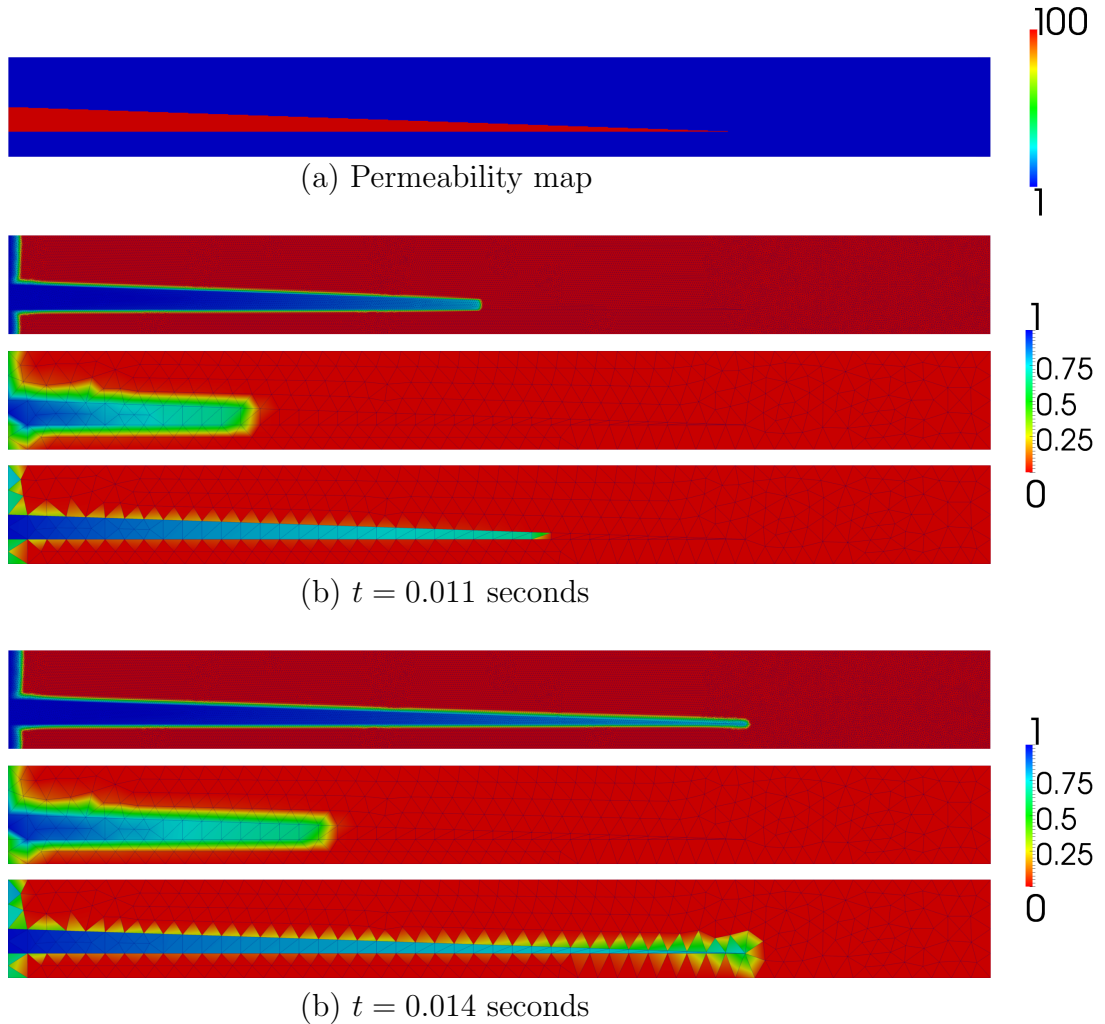
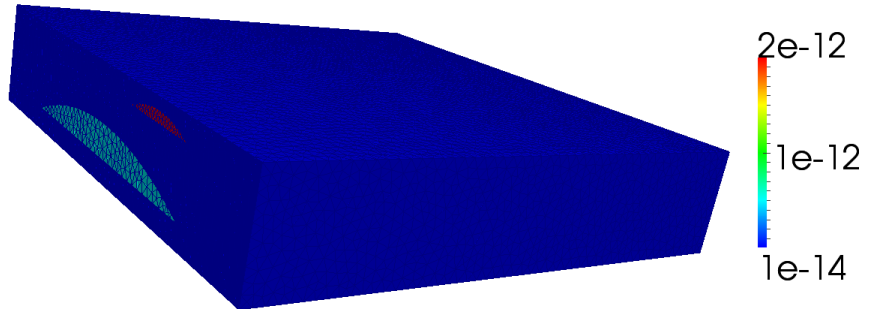
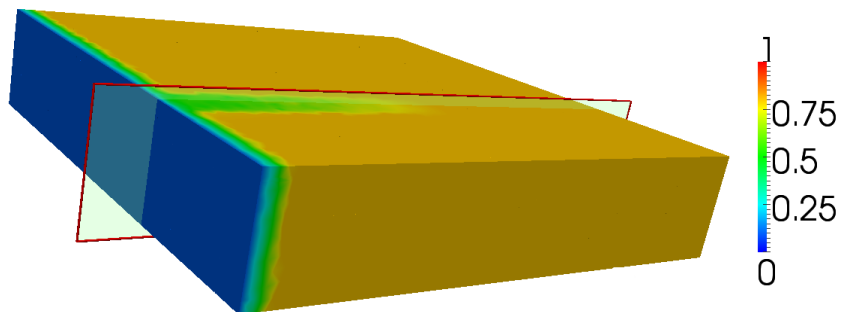


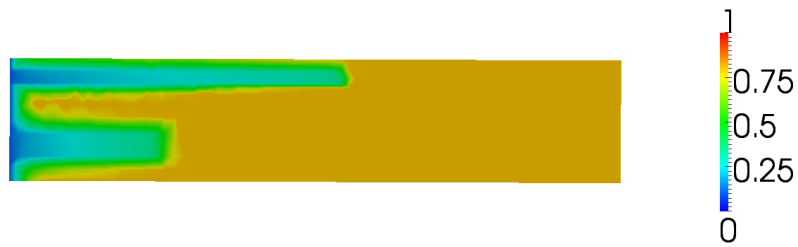
Figure 14: Wedged-shaped region: (a) two phase flow in a rectangular domain with an internal wedge-shaped region with high-permeability. Snapshots of water-phase saturation profiles of simulations performed with a fine mesh P_0 DG- P_1 simulation (top) and course mesh P_0 DG- P_1 simulation (middle) and course mesh P_2 DG- P_1 DG simulation (bottom) at (b) 0.011 and (c) 0.0014 seconds.



(a) Permeability map



(b) $t = 7.9$ years



(c) Internal section

Figure 15: Hexahedron domain: (a) Permeability map and mesh used. Snapshots of water-phase saturation profiles of simulations performed with P_0DG-P_1 (b) 3-D solution and (c) 2-D internal slice.